Aerodynamic damping during rapid flight maneuvers in the fruit fly *Drosophila*

B. Cheng[1], S. N. Fry[2], Q. Huang[3] and X. Deng[1,*]

[1]School of Mechanical Engineering, Purdue University, Zucrow Laboratories, West Lafayette, IN 47907, USA, [2]Institute of Neuroinformatics and Institute of Robotics and Intelligent Systems, University of Zurich and ETH Zurich, Switzerland and [3]Department of Mechanical Engineering, University of Delaware, 126 Spencer Laboratory, Newark, DE 19716, USA

*Author for correspondence (xdeng@purdue.edu)

SUMMARY

We systematically investigated the effect of body rotation on the aerodynamic torque generation on flapping wings during fast turning maneuvers (body saccades) in the fruit fly *Drosophila*. A quasi-steady aerodynamic simulation of turning maneuvers with symmetrically flapping wings showed that body rotation causes a substantial aerodynamic counter-torque, known as flapping counter-torque (FCT), which acts in the opposite direction to turning. Simulation results further indicate that FCTs are linearly dependent on the rotational velocity and the flapping frequency regardless of the kinematics of wing motion. We estimated the damping coefficients for the principal rotation axes – roll, pitch, yaw – in the stroke plane frame. FCT-induced passive damping exists about all the rotation axes examined, suggesting that the effects of body rotation cannot be ignored in the analysis of free-flight dynamics. Force measurements on a dynamically scaled robotic wing undergoing realistic saccade kinematics showed that although passive aerodynamic damping due to FCT can account for a large part of the deceleration during saccades, active yaw torque from asymmetric wing motion is required to terminate body rotation. In addition, we calculated the mean value of the damping coefficient at 21.00×10^{-12} N m s based on free-flight data of saccades, which is somewhat lower than that estimated by the simulation results (26.84×10^{-12} N m s).

Key words: *Drosophila*, flight dynamics, saccade, aerodynamics, damping, flapping counter-torque.

INTRODUCTION

Insects are capable of elaborate flight maneuvers that outperform other flying animals and technical devices alike. The physiological and biomechanical basis of flapping flight have been explored for decades (Collett and Land, 1975; Ellington, 1984a; Ennos, 1989; Dudley, 1990; Dudley, 1991). In recent years, technological and methodological advances, such as dynamic force scaling using robotic wings (Dickinson et al., 1999; Sane, 2001; Fry et al., 2003), high-speed videography (Fry et al., 2003; Fry et al., 2005; Hedrick, 2008), and computational fluid simulations (Ramamurti and Sandberg, 2002; Sun and Xiong, 2005), have significantly advanced knowledge of insect flight aerodynamics. This knowledge provides the basis for further exploration of the dynamics and control of flapping flight, which is relevant to the underlying neuromotor control principles and biomimetic design of micro air vehicles (MAVs).

Flight dynamics and control mechanisms have been particularly well studied in flies, whose rich behavioral repertoire is amenable to detailed analysis both in free (e.g. Collett and Land, 1974; Land and Collett, 1975; Schilstra and Van Hateren, 1999; Fry et al., 2003; Fry et al., 2005; Fry et al., 2008; Ribak and Swallow, 2007) and tethered (e.g. Heisenberg and Wolf, 1979; Götz, 1987; Heisenberg and Wolf, 1988; Taylor and Thomas, 2003; Fry et al., 2005; Bender and Dickinson, 2006a; Hesselberg and Lehmann, 2007) flight. Flies exhibit a characteristic flight behavior that consists of prolonged segments of straight flight, interrupted by brisk turning maneuvers termed body saccades (Collett and Land, 1975; Tammero and Dickinson, 2002; Fry et al., 2003). During a saccade, a fruit fly subtly modulates its wing kinematics to produce the required aerodynamic torque to induce the quick changes in body posture characteristic of a banked turn (Fry et al., 2003; Fry et al., 2005). It was previously assumed that the flight dynamics of insects are highly overdamped because viscous effects eventually dominate at small size scales. Under this assumption, an insect would need to generate aerodynamic torque from an asymmetric wing stroke to overcome the viscous drag acting on the body throughout the turn. Time constants (ratio of inertia and damping coefficient) for the damping of body rotation were estimated to range between 4 and 20 ms even in considerably larger, and hence more inertial, fly species (Collett and Land, 1975; Reichardt and Poggio, 1976a; Reichardt and Poggio, 1976b) [but see Mayer et al. for *Drosophila* (Mayer et al., 1988)].

Inconsistent with the notion of dominant viscous body drag, high-speed recordings of free-flying *Drosophila* showed that even these tiny flies steered in the direction of the turn only during the first half of the saccade, but then tended to steer in the opposite direction even while the angular speed remained high [see figure 3C,F in Fry et al. (Fry et al., 2003)]. A Stokes' estimate showed that body friction could not account for the termination of body rotation, which instead was attributed to active counter-steering by the fly (i.e. active counter-torque due to asymmetries of wing motion). Because the wing kinematics were measured in a body frame (i.e. the measurements were performed with a dynamically scaled flapping wing that did not reproduce the rotation of the fly's body), the possible contribution of passive wing damping, i.e. the counter-torque induced by symmetric wing kinematics in the presence of body rotation, was not considered in Fry and colleagues' study. More recently, Hesselberg and Lehmann estimated a time constant of 9.6 ms [calculated based on Hesselberg and Lehmann (Hesselberg and Lehmann, 2007)] for *Drosophila*, based on a behavioral analysis of tethered flight and a damping model based on a time-averaged analysis of aerodynamic wing torques. They concluded that passive frictional damping acting on the wings dominates flight dynamics during saccades.

A clear understanding of the origin and mechanisms of damping is relevant in a broader context of flight stability. Taylor and Thomas analyzed the longitudinal stability of tethered *Schistocerca gregaria* under disturbance from the environment (Taylor and Thomas, 2003). Sun and colleagues, likewise, studied the longitudinal passive stability of a hovering model insect by the Computational Fluid Dynamics (CFD) method in the absence of active control (Sun and Xiong, 2005; Sun and Wang, 2007). Despite the differences between these two approaches and their results, both studies identified unstable modes in the flight dynamics. Sun and Xiong further indicated that the instability arises from a coupling of nose-up pitching with forward horizontal motion (and nose-down pitching with backward horizontal motion) (Sun and Xiong, 2005). Collectively, although previous work on insect flight stability is mostly related to longitudinal dynamics, and a comprehensive analysis is absent, it is widely believed that insect flight is inherently unstable, and active control of wing kinematics is essential to achieve stable flight. The controversial views relating to the effects of passive damping and active flight control warrant a detailed analysis of the aerodynamic mechanisms underlying passive wing damping during maneuvers.

In this study, we systematically investigated the effect of body angular velocity on aerodynamic force and torque production, and we arrived at a comprehensive explanation for the mechanism of passive aerodynamic damping due to flapping counter-torque (FCT) production. We start with a quasi-steady aerodynamic analysis to quantitatively address the passive damping effect due to body rotation about the yaw axis in the stroke plane, and then extend our analysis to roll and pitch axes in the stroke plane frame. Using a dynamically scaled robotic wing, we measured the effect of passive damping based on previously measured free-flight saccade kinematics (Fry et al., 2003). We estimated damping coefficients and time constants based on both simulation results and experiments to quantitatively assess the effects of passive aerodynamic damping in turning flight. We conclude that FCT plays a significant role in decelerating body rotation during a saccade, but that active control from asymmetric wing motion is additionally required to stabilize the body at the end of a saccade.

MATERIALS AND METHODS
Simulations based on quasi-steady aerodynamic models

The coordinate system and kinematic parameters used throughout this paper are summarized in Fig. 1. A stroke plane coordinate frame (x_s, y_s, z_s) is introduced to provide a reference frame for wing kinematics and angular velocities of the fly, for which we assumed a horizontal stroke plane at the start of each simulation. The body frame x_b, y_b, z_b is oriented with a fixed pitch angle (free body angle χ_0) from the stroke plane frame, and the two frames share a common origin located at the center of mass. Wing kinematics are described by Euler angles, termed stroke position (ϕ), deviation (θ) and rotation angle (φ). For simplification, the head, thorax and abdomen of the fruit fly are modeled as ellipsoids (Fig. 1). The mass and inertia matrix are calculated based on the measured morphological data of the fruit fly *Drosophila* [see appendix C of Cheng et al. (Cheng et al., 2009)].

In the current study, we considered the translational component (due to delayed stall) of the aerodynamic force to be a dominant factor in FCT production and ignored the effect of rotational lift (due to the Kramer effect) and wake capture (Sane, 2001). The rotational force component does not render a better prediction of force transients, although it does slightly increase the mean total force so it is closer to the measured value for real flies (Fry et al., 2005). We first calculated the time-continuous aerodynamic forces
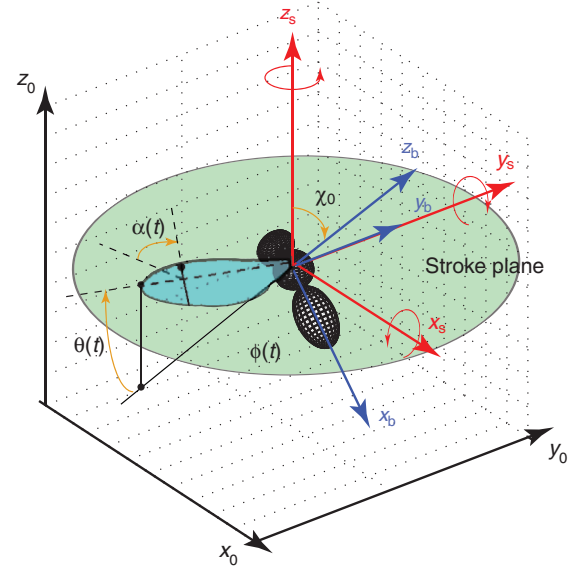

Fig. 1. Fruit fly model. The corresponding morphological data are presented in appendix C of Cheng et al. (Cheng et al., 2009). Head, thorax and abdomen are modeled as ellipsoids. Thorax and abdomen are aligned with the body roll axis x_b, while the misalignment of the head with respect to the thorax is 30 deg. The stroke plane frame (x_s, y_s, z_s) is fixed with respect to the body frame with a constant free body angle χ_0 of 45 deg. (Fry et al., 2005), and shares the same origin at the center of mass of the fly. Wing kinematics are specified by three Euler angles; stroke position (ϕ), deviation (θ) and rotation angle (φ). Angle of attack (α) is defined as the angle of the wing chord and the tangential of the wing's trajectory [rotation angle φ is not shown in this figure due to inconvenient representation; for details of Euler angle please refer to Murray et al. (Murray et al., 1994)]. Unless otherwise mentioned, this paper follows the conventions and nomenclature of Sane and Dickinson (Sane and Dickinson, 2001). The rotations are simulated individually about the three principal axes in the stroke plane frame (red arrows).

acting on each wing; and then calculated the corresponding aerodynamic torques about each principal axis assuming a center of pressure located at 70% along the wing span (Sane, 2001; Ramamurti and Sandberg, 2002; Fry et al., 2005).

Although it is often observed that a saccade is coupled by non-zero translational body velocities, in this study we only considered the turning flight dynamics with zero reduced frequency (body velocity/wing velocity) under symmetric wing kinematics. We used 'U-shaped' wing kinematics (Fig. 2A) that closely mimicked those previously measured in freely hovering *Drosophila* (Fig. 3A) (Fry et al., 2005) with a wingbeat frequency of 212 Hz. To explore how wing motions affect FCT production, we additionally tested six sets of artificial wing kinematics modeled by sinusoids: stroke angle $\phi(t)=(\Phi/2)\cos(nt)$, stroke deviation $\theta(t)=(\Theta/2)\cos(2nt+\beta)+\Theta_0$ and rotation angle $\varphi(t)=45\,\text{deg.sin}(nt)$ (stroke parameters listed in Table 1B–G and Fig. 2B–G). Rotations were simulated individually about the three principal axes (roll, pitch, yaw) of the stroke plane frame (Fig. 1).

First, to analyze the passive damping effect during a saccade, we simulated the rotation about the stroke plane's yaw axis (z_s). Note, the current study assumed a 'pure' yaw rotation about the principal axis, which ignored the rolling and pitching motion during realistic saccades. Despite these factors, we expect the simplified simulations to capture the major characteristics of a saccade. We used a turning velocity of 2000 deg. s^{-1}, which is close to the average yaw velocity previously measured during a saccade [see figure 2 in Fry et al.
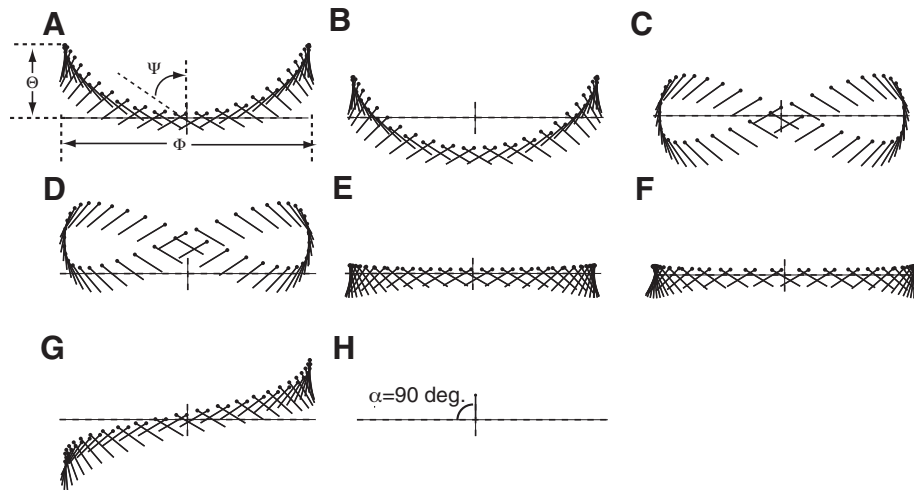
Fig. 2. Schematic representations of wing kinematics used in simulation. Black line denotes the wing chord, with a dot marking the leading edge. The stroke parameters are listed in Table 1. (A) 'U-shaped' wing trajectory representing a simplified version of kinematics measured in free-flying *Drosophila* (Fig. 3A). Also plotted are schematic representations of stroke amplitude Φ, maximum deviation Θ and rotation angle Ψ (45 deg.). (B) U-shaped wing trajectory without a stroke deviation offset. (C) 'Figure of 8-shaped' wing trajectory without a stroke deviation offset. (D) Figure of 8-shaped wing trajectory with a stroke deviation offset of 30 deg. Kinematics E and F have different stroke amplitudes but both are without stroke deviation. G has a maximum stroke deviation of 30 deg. at the stroke reversals, and varies linearly in between. H represents wing motion with the wing fixed at body frame at the middle of the stroke, and sweeping through the air at an angle of attack of 90 deg. Note that the vertical dimension is not shown to scale with the horizontal dimension.

(Fry et al., 2003)]. We then calculated the instantaneous total yaw torque (together with roll and pitch torque) produced by both wings, which is now known as flapping counter-torque from a parallel study (FCT) (Cheng et al., 2009; Hedrick et al., 2009). It acts in the opposite direction of rotation and leads to passive aerodynamic damping. For comparison, we also calculated the resultant aerodynamic torque with both wings stationary with respect to the stroke plane at a constant angle of attack of 90 deg. (Fig. 2H) (maximum normal force acting on the wing is expected), using the same turning angular velocity. Without wing flapping, the wing

velocity is induced solely by the turning velocity. Because the aerodynamic force is proportional to wing velocity squared (Dickinson et al., 1999), we expect the corresponding counter-torque to be proportional to the turning velocity squared. However, with wing flapping, FCT arises from a subtractive effect due the asymmetry of wing motion (see following section) and it is linearly dependent on turning velocity.

To see whether a similar FCT effect exists under other types of body rotation, we then repeated the above simulations for rotations about the remaining principal axes in the stroke plane frame (x_s and
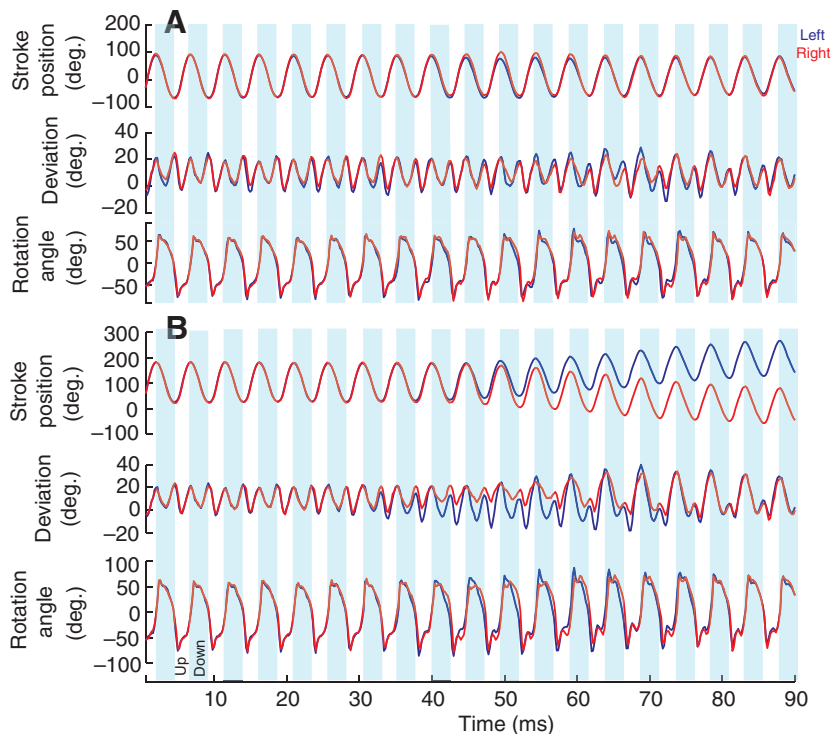

Fig. 3. Instantaneous wing kinematics used in the robotic wing experiments (stroke position ϕ, deviation θ and rotation angle φ; for definitions see Fig. 1). (A) Wing kinematics in body-centered frame of the left (blue) and right (red) wing re-plotted from Fry et al. (Fry et al., 2003). (B) Wing kinematics in the inertial frame (taking body rotation into consideration) of the left (blue) and right (red) wing. Wing kinematics in the body-centered frame are derived as the *ZYX* Euler angle sequence for coordinate transformation from the stroke frame to the wing frame; wing kinematics in the inertial frame are derived as the *ZYX* Euler angle sequence for coordinate transformation from the inertial frame to the wing frame. For details of derivation please refer to Murray et al. (Murray et al., 1994).

Table 1. Wing kinematics used in the simulation

Kinematics set	Stroke amplitude Φ (deg.)	Deviation amplitude Θ (deg.)	Deviation timing β (deg.)	Deviation offset Θ_0 (deg.)
A	140	30	0	15
B	140	30	0	0
C	140	30	90	0
D	140	30	90	15
E	140	0	0	0
F	180	0	0	0
G	140	Deviation linearly varies with stroke position		

Values for the stroke amplitude Φ, deviation amplitude Θ, deviation offset Θ_0, and deviation timing β are listed.

y_s, Fig. 1), and calculated the respective torques about all three principal axes. For roll and pitch rotation, we also chose angular velocities close to the mean values observed in free flight (ω_{xs}=2000 deg. s^{-1}, ω_{ys}=1000 deg. s^{-1}).

Finally, we explored how turning velocity and flapping frequency affect FCTs. For each type of rotation (roll, pitch and yaw), we used two consecutive simulation series: a turning velocity series, in which turning velocity is varied from –3000 to 3000 deg. s^{-1}, while flapping frequency is fixed at 212 Hz; a flapping frequency series, in which flapping frequency is varied from 0 to 318 Hz while turning velocity is fixed at 2000 deg. s^{-1}.

Theoretical estimations of damping coefficients
The mechanism of FCT can be quantitatively explained using quasi-steady models and a few simplifying assumptions. First, the aerodynamic forces on the wing are largely described by translational components due to delayed stall (Dickinson et al., 1999). The aerodynamic force is approximately proportional to the square of wing velocity, which is due to inertial fluid effects, such as delayed stall, rather than viscous effects, such as friction. This is consistent with recent studies that have shown inertial fluid effects to dominate over viscous effects at Reynolds numbers between 10^2 and 10^3 (Sane, 2001). Second, we assume that the moment arms (defined as the vector from the center of mass of the body to the center of pressure on the wing) for the two wings are the same, allowing us to uniformly describe the instantaneous yaw torques in the stroke plane during upstrokes and downstrokes. A mathematical derivation of FCT during yaw rotation (stroke plane frame of reference) is presented in Cheng et al. (Cheng et al., 2009) [also refer to supporting material in Hedrick et al. (Hedrick et al., 2009)]. The instantaneous FCT about the yaw axis (z_s) is written as:

$$\tau_{\text{yaw}}(\hat{t}) = -C_D(\hat{t})\rho R^4 \bar{c} \hat{r}_2^2 (S) \hat{r}_{\text{cp}} \Phi n \left|\frac{d\hat{\phi}}{d\hat{t}}\right| \omega_{zs}$$

$$\approx -C_N(\hat{t})\rho R^4 \bar{c} \hat{r}_2^2 (S) \hat{r}_{\text{cp}} \Phi n \cos(\varphi) \left|\frac{d\hat{\phi}}{d\hat{t}}\right| \omega_{zs} , \quad (1)$$

while the stroke-averaged value is:

$$\overline{\tau_{\text{yaw}}} = -\rho R^4 \bar{c} \hat{r}_2^2 (S) \hat{r}_{\text{cp}} \Phi n \overline{C_N(\hat{t}) \cos(\varphi) \left|\frac{d\hat{\phi}}{d\hat{t}}\right|} \omega_{zs} , \quad (2)$$

where ρ is air density, R is wing length, $\bar{c}$ is mean chord length, $C_D(\hat{t})$ is the instantaneous drag coefficient at non-dimensional time $\hat{t}$ (Dickinson et al., 1999), which is approximated by $C_N(\hat{t})\cos(\varphi)$, $C_N(\hat{t})$ is the instantaneous normal force coefficient (Deng et al., 2006), φ is wing rotation angle (for simplicity we have assumed φ is symmetric for left and right wings), $d\hat{\phi}/d\hat{t}$ is the normalized wing angular velocity, ω_{zs} is the angular velocity about the stroke plane yaw axis, Φ and n are wing flapping amplitude and frequency, $\hat{r}_2^2(S)$

is the non-dimensional second moment of wing area and $\hat{r}_{\text{cp}}$ is the normalized center of pressure on the wing. The stroke-averaged roll and pitch torques are expected to be zero:

$$\overline{\tau_{\text{roll}}} = \overline{\tau_{\text{pitch}}} = 0 , \quad (3)$$

Eqns 1 and 2 suggest that the FCT is proportional to both angular velocity ω_{zs} (the component perpendicular to the stroke plane) and wing flapping frequency n. Note that although body frictional damping and FCT-induced damping both depend linearly on the angular velocity, the underlying aerodynamic mechanisms for FCT production are in fact quite different. Body friction is a low Re frictional effect and as such depends linearly on the angular body velocity. FCT, in contrast, depends linearly on the angular body velocity due to a subtractive effect of the two wings beating in opposite directions (Tobalske, 2009). These conclusions will be further validated by systematically varying these two parameters (see end of this section).

Since it is reasonable to view FCT as a form of aerodynamic damping due to its linear relationship with angular velocity, here we define the FCT aerodynamic damping coefficient as:

$$C_{i-j} = -\frac{\overline{\tau_{i-j}}}{\omega_j} , \quad (4)$$

where i represents the axis for which the torque and the angular velocity are specified and j represents the rotation axis. For example, τ_{xs-zs} represents the torque about the roll axis (x_s) during yaw (z_s) rotation; ω_j represents the averaged angular velocity about the specified rotation axis j.

Next, based on Eqns 1–3, we can estimate the damping coefficients during rotation about the stroke plane's roll, pitch and yaw axis:

$$C_{xs-zs} = -\frac{\overline{\tau_{xs-zs}}}{\omega_{zs}} = 0 , \quad (5)$$

$$C_{ys-zs} = -\frac{\overline{\tau_{ys-zs}}}{\omega_{zs}} = 0 , \quad (6)$$

$$C_{zs-zs} = -\frac{\overline{\tau_{zs-zs}}}{\omega_{zs}} = \frac{\rho R^4 \bar{c} \hat{r}_2^2 (S) \hat{r}_{\text{cp}} \Phi n \overline{C_N(\hat{t}) \cos(\varphi) \left|d\hat{\phi}/d\hat{t}\right|} \omega_{zs}}{\omega_{zs}} . \quad (7)$$

Experimental setup
The experimental setup used in this study was similar to one described in Zhao et al. (Zhao et al., 2009). We used a bevel-geared robotic wrist to generate rotational motion about three orthogonal axes. The drive shafts were powered by 16 mm, 0.3 N m torque DC brush motors (Maxon Motor AG, Sachseln, Switzerland) equipped with gear heads to reduce speed and magnetic encoders to provide

kinematic feedback to ensure motion fidelity. The motors were driven according to kinematic patterns provided by a custom-written Matlab Simulink program (The Mathworks, Natick, MA, USA) with WinCon software (Quanser Consulting, Ontario, Canada). This software provided commands to the real-time control and data acquisition board (Q8, Quanser Consulting, Ontario, Canada) communicating with the hardware. We used proportional-integral-derivative (PID) controllers to run the motors with a precision of 0.1 deg. Motion commands from the computer were amplified by analog amplifier units (Advanced Motion Controls, CA, USA) that directly controlled the input current received by the motors. Wings were made of plastic sheet PET-G (thickness of 0.06 in, 1.52 mm) with the shape of a fruit fly wing and a length of 18 cm. The wing base was attached to a holder affixed on the gear box. The instantaneous force and torque acting on the wing were measured using a six-component force–torque sensor (ATI NANO-17, Apex, NC, USA) attached to the wing holder. The wing along with the gearbox (2.54 cm×2.54 cm×2.54 cm) were immersed in a tank (46 cm width×41 cm height×152 cm length) filled with mineral oil (kinematic viscosity $\approx$20 cSt at 20°C, density $\approx$850 kg m^{-3}).

This overall set-up enabled us to move the wings along pre-determined stroke paths and simultaneously measure the resulting fluid dynamic forces acting on each wing. We calculated the Reynolds number for our experiments at 250 from the equation:

$$\overline{Re} = \frac{4\Phi R^2 n}{\nu(AR)} , \tag{8}$$

where AR is the aspect ratio, n is the wing beat frequency, R is wing length, Φ is the stroke amplitude and ν is the kinematic viscosity of the fluid (Ellington, 1984b). Although the Reynolds number for a flapping wing in hovering *Drosophila* is somewhat lower at 150 (Fry et al., 2003; Fry et al., 2005), we expect this difference to have negligible effects on force generation, as confirmed by both CFD simulation and previous Robofly experiments (see also Sane, 2001; Sane, 2002).

Experiments and estimation of yaw torque based on fruit fly saccade data

Based on the free-flight saccade data previously recorded by Fry and colleagues (Fry et al., 2003), we first estimated the damping coefficient based on Eqn 7. Next, we validated our simulation results with experiments using a set of saccade data measured under almost perfect hovering conditions (mean and maximum reduced frequency at 0.012 and 0.031, respectively), which makes it ideal for exploring the aerodynamic mechanisms pertaining to turning maneuvers without the complications arising from an additional translational component. For the same reason, these data were used for a CFD study (Ramamurti and Sandberg, 2007), the results of which will also be compared with those of the present work. From these specific saccade data, we extracted two sets of wing kinematics. The first kinematics (Fig. 3A) were extracted with respect to the body-centered frame and are identical to the ones used by Ramamurti and Sandberg (Ramamurti and Sandberg, 2007). The second set (Fig. 3B) is extracted with respect to the inertial frame, which takes into consideration the body rotation (but not the translational body velocity). We played the above two sets of wing kinematics on the robotic wing and evaluated the effect of body rotation on the aerodynamic force and torque production of the wing.

We assumed wing–wing interactions are negligible because no 'clap-and-fling' behavior was observed in free-flying *Drosophila* (Fry et al., 2003; Fry et al., 2005). Therefore, measurements were performed with a single robotic wing. Forces and torques are first measured in wing-centered coordinates. The forces measured on the robotic wing are corresponding to scaled up versions of those on the real fly's wings, according to the force scaling rule (Appendix 1). The total torque in the body frame was then obtained through coordinate transformation.

In addition, torques in the body frame could be estimated based on the insect body kinematics: if the insect body is modeled as a rigid body, its complete dynamics are described by the Newton–Euler equations of motion (Murray et al., 1994):

$$\begin{bmatrix} m\mathbf{I} & 0 \\ 0 & \mathbf{T} \end{bmatrix} \begin{bmatrix} \dot{\mathbf{v}}^b \\ \dot{\boldsymbol{\omega}}^b \end{bmatrix} + \begin{bmatrix} \boldsymbol{\omega}^b \times m\mathbf{v}^b \\ \boldsymbol{\omega}^b \times \mathbf{T}\boldsymbol{\omega}^b \end{bmatrix} = \mathbf{F}^b =$$

$$\begin{bmatrix} \mathbf{f}_a \\ \boldsymbol{\tau}_a \end{bmatrix} + \begin{bmatrix} \mathbf{f}_f \\ \boldsymbol{\tau}_f \end{bmatrix} + \begin{bmatrix} \mathbf{f}_g \\ 0 \end{bmatrix} , \tag{9}$$

where m is the body mass, $\mathbf{I}$ is the identity matrix, $\mathbf{T}$ is the body moment of inertia matrix, and $\boldsymbol{\omega}^b$ and $\mathbf{v}^b$ are the instantaneous body frame angular and translational velocities. $\mathbf{F}^b$ is the total wrench acting on the body [for definition of wrench refer to Murray et al. (Murray et al., 1994)]. The terms $\mathbf{f}_a$ and $\boldsymbol{\tau}_a$ represent the aerodynamic forces and torques; $\mathbf{f}_f$ and $\boldsymbol{\tau}_f$ are the frictional damping forces and torques acting on the fly's body, and $\mathbf{f}_g$ is the body gravitational force. The gravitational force of the wing is much smaller than the other components and is thus ignored. The quantities on the left-hand side of the equation were calculated based on the body kinematics and morphology data described in appendix C of Cheng et al. (Cheng et al., 2009). Theoretically, the time trace of the estimated quantities on the left side (predicted force and torque) and those measured on the right side of the equation should match the bounded discrepancies, which arise from measurement errors and uncertainties in the morphological parameters (see also Discussion).

RESULTS
FCT-induced damping during body rotation

We first simulated rotation about the yaw axis z_s (stroke plane frame) with the wings fixed at an angle of attack of 90 deg. (Fig. 2H). The calculated counter-torque was 3.62×10^{-11} N m. With the wings flapping symmetrically (with simplified realistic fruit fly wing kinematics, Fig. 2A) under otherwise identical conditions, the stroke-averaged FCT was 9.37×10^{-10} N m (instantaneous and mean values are summarized in Fig. 4A–C), a roughly 26-fold increase compared with the non-flapping case. Aerodynamic counter-torque was therefore greatly enhanced by the flapping motion of the wing. The magnitude of this counter-torque is about half of the maximum body frame yaw torque of 2×10^{-9} N m resulting from active turning, i.e. due to asymmetric wing motion (Fry et al., 2003). Therefore, the aerodynamic damping due to FCT is at least partially responsible for the deceleration during saccades in the form of a passive damping, suggesting that only a small additional amount of active counter-torque is required to terminate body rotation and finally stabilize the body orientation.

Based on the above simulations, the estimated yaw damping coefficient C_{zs-zs} is 26.84×10^{-12} N m s, while C_{xs-zs} and C_{ys-zs} are both zero as predicted by Eqns 5 and 6, indicating that the direction of FCT is collinear with the rotation axis. To compare the role of inertia and damping in flight dynamics during turning, we investigated the dynamics in the body coordinate frame. Here we assumed that the turning velocity is confined to the vertical axis (stroke plane yaw axis z_s), and the stroke plane is horizontal. We

Fig. 5. Pitch torque over half of a stroke cycle (abscissa) for the simulated rotation about the pitch axis y_s. Torques during up (blue) and down (red) strokes are plotted together for comparison. The total pitch torque is shown in green with its mean value (filled green cycles on the ordinates).
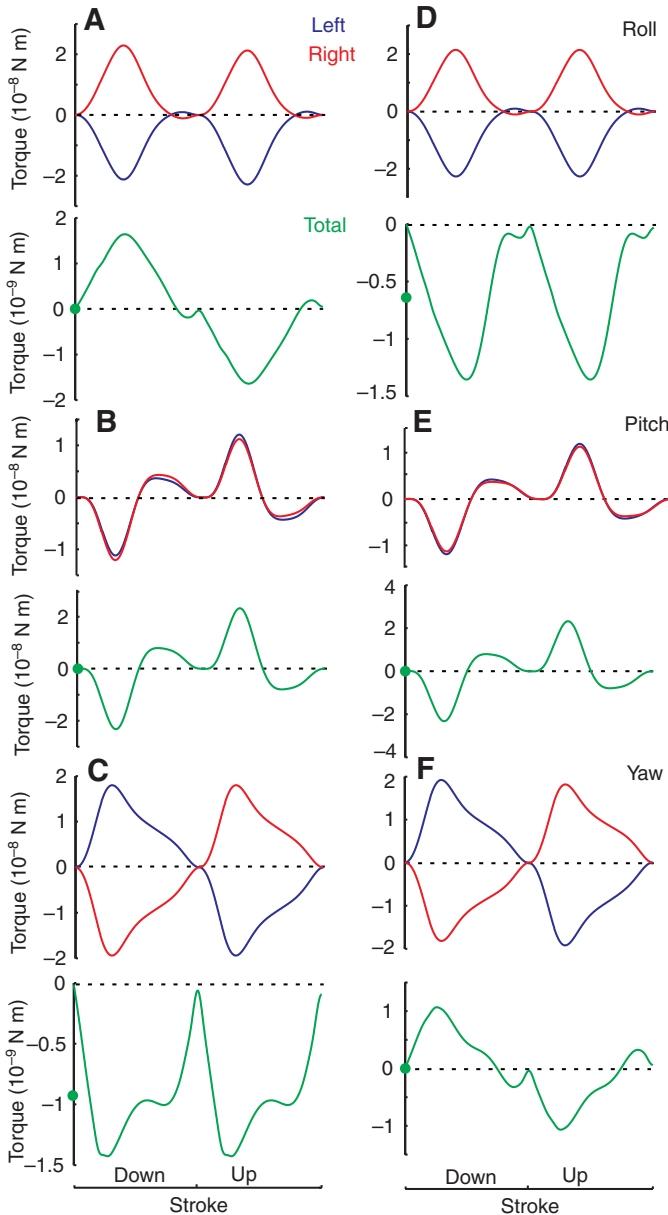

Fig. 4. Torques for the simulated rotation about the yaw and roll axes. (A–C) Roll, pitch and yaw torques of the left (blue) and right (red) wing for rotation about the yaw axis z_s. The total yaw torque is shown in green with its mean value (filled green cycles on the ordinates). (E–G) Roll, pitch and yaw torques for rotation about the roll axis x_s. The same notation is used as in A–C.

flight data of a saccade (Fry et al., 2003), and only examined the body frame yaw dynamics, which simplifies to [for details see appendix A in Cheng et al. (Cheng et al., 2009)]:

$$I_{yaw}\dot{\omega}_{yaw}^b = \tau_{active} - \tau_{FCT} - \tau_{friciton}$$
$$= \tau_{active} - C_{zb-zs}\omega_{zb} - C_{friction}\omega_{zb} , \qquad (10)$$

where τ_{active} is the active component of yaw torque, τ_{FCT} is the passive yaw counter-torque due to FCT (torques in Eqn 10 are about body yaw axis z_b; it can be obtained by a projection from the torque about z_s), I_{yaw} is the yaw moment of inertia estimated from body morphology [4.971×10^{-12} N m s^2 in appendix C of Cheng et al. (Cheng et al., 2009)], ω_{zb} is the rotational velocity projected to the body yaw axis during turning, and $C_{friction}$ is the frictional damping coefficient of the body. The total damping coefficient, $C_{zb-zs}+C_{friction}$, was estimated as 27.36×10^{-12} N m s. $C_{friction}$ was estimated by Stokes' law [0.52×10^{-12} N m s in Fry et al. (Fry et al., 2003)], whereas the FCT component C_{zb-zs} was calculated as 26.84×10^{-12} N m s (equal to the value of C_{zs-zs} by definition (Eqn 4) and the fact that FCT is collinear with the rotation axis), more than 50 times the value of body frictional damping.

In addition to the rotation about the yaw axis, we also simulated the situation in which the fly is rotating separately about the roll (x_s) and pitch (y_s) axes (Fig. 1). The results show similar FCTs during these rotations. Fig. 4D–F shows the time courses of torque generation during roll rotation. A roll counter-torque is observed by summing the torque of the left and right wing, and, similar to the situation during yaw rotation, the only non-zero stroke-averaged torque is about the roll axis. During the pitch rotation, left and right wings have symmetric wing kinematics at any instant of time; therefore zero resultant roll and yaw torques are expected (not plotted here). However, a pitch counter-torque arises by comparing the torque generation between upstrokes and downstrokes (Fig. 5). Together with the yaw rotation, the corresponding damping coefficients calculated based on Eqn 4 are summarized in Table 2.

Besides the realistic fruit fly wing kinematics, we also used six artificial sets of wing kinematics to simulate yaw rotation (as

artificially separated the total yaw torque into an active component, which is due to asymmetric wing motion [i.e. without body rotation, as in Fry et al. (Fry et al., 2003)] and a passive component (FCT damping and body friction combined). Note that aerodynamic forces are highly non-linear functions of wing angle of attack that depend on the continuous interactions between the oscillating wing and the surrounding air. The artificial separation of active and passive torque components serves to illustrate the underlying mechanisms based on the chosen simplified assumption. Here we neglected the cross-product terms in Eqn 9, since the magnitude of the cross-term is near 3.5% of the value of the other terms calculated based on free-
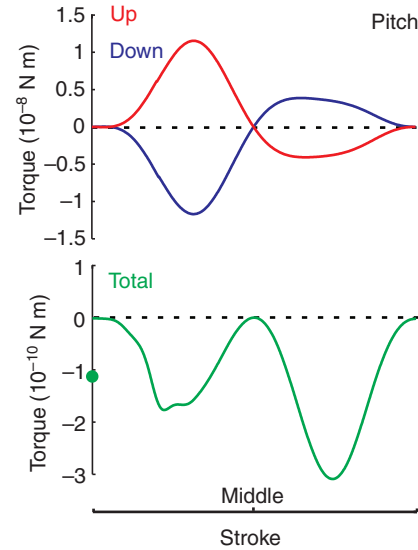
Table 2. Damping coefficients (dimension: 10^{-12} N m s) for different wing kinematics and rotation axes

Kinematics set	Roll rotation			Pitch rotation			Yaw rotation		
	C_{xs-xs}	C_{ys-xs}	C_{zs-xs}	C_{xs-ys}	C_{ys-ys}	C_{zs-ys}	C_{xs-zs}	C_{ys-zs}	C_{zs-zs}
A	18.33	0	0	0	6.42	0	0	0	26.84
B	15.41	0	0	0	7.74	0	0	0	28.93
C	19.77	−0.06	0	0	3.20	0	0	−0.06	30.80
D	19.88	−0.06	0	0	4.42	0	0	−0.06	28.13
E	12.98	0	0	0	4.36	0	0	0	29.56
F	14.21	0	0	0	8.08	0	0	0	38.02
G	15.78	0	7.88	0	5.32	0	7.25	0	28.48

Note that a positive damping coefficient corresponds to a negative (counter) torque and *vice versa*. For definitions of rotation axes refer to Fig. 1.

described in Fig. 2B–G). The resulting damping coefficients are documented in Table 2. Additionally, Fig. 6 illustrates the instantaneous yaw counter-torque using the wing kinematics B, C, E and G. From Table 2, it can be seen that 'figure of 8-shaped' wing kinematics generally generate stronger roll and yaw damping, but less pitch damping compared with the 'U-shaped' wing kinematics. A comparison of the results obtained using the kinematics E and F shows that pitch damping is substantially enhanced by increasing the stroke amplitude, while roll and yaw damping are also enhanced. Table 2 also indicates that, for all sets of wing kinematics, yaw rotation produced the strongest damping, while pitch rotation produced the least.

Moreover, except for kinematics G (which resembles flapping under a tilted stroke plane), the kinematics (A–F) show damping (due to FCT) that is most prominent about the rotation axes (values of counter-torques about other axes are zero or negligible). In other words, FCTs are roughly collinear with the turning axes. Notably, this is also true for rotations about x_b and z_b axes [not shown here (see Cheng et al., 2009)], which have an oblique orientation with respect to the stroke plane frame coordinates with a fixed pitch angle χ_0. Thus, it seems likely that FCT occurs for any rotation axis.

Remarkably, although aerodynamic forces and torques are inherently non-linear functions of body velocity (both linear and angular) and wing kinematics, the FCT model (Eqns 1 and 2) predicts that, during yaw rotation, FCT is linearly dependent on the rotational velocity and flapping frequency. Therefore, we systematically varied the flapping frequency and rotational velocity to quantify their effects on FCT and test for its linearity. The results based on simplified fruit fly wing kinematics are shown in Fig. 7. Apparently,

for all the rotation axes, the resultant FCTs linearly increase with the angular velocities and flapping frequencies, indicating the corresponding damping coefficients are constants under different conditions. Therefore, the magnitudes of the slope in Fig. 7A are expected to be the value of damping coefficients for each simulated rotation. Notably, the above linearity is also true for the other six sets of wing kinematics (result for wing kinematics B–G not shown).

Note that, the mathematical model of FCT ignored stroke deviation [see appendix B in Cheng et al. (Cheng et al., 2009)]. However, the current results show that linearity is maintained in the presence of varying timing of wing rotation deviation offsets. The linear dependence of FCT on flapping frequency and rotational velocity therefore appears be a basic feature of flapping flight, regardless of the particular wing kinematics. In a parallel study, the FCT model has successfully predicted the deceleration time in wingbeat time scale across seven different species with distinct wing kinematics, and body and wing morphologies (Hedrick et al., 2009).
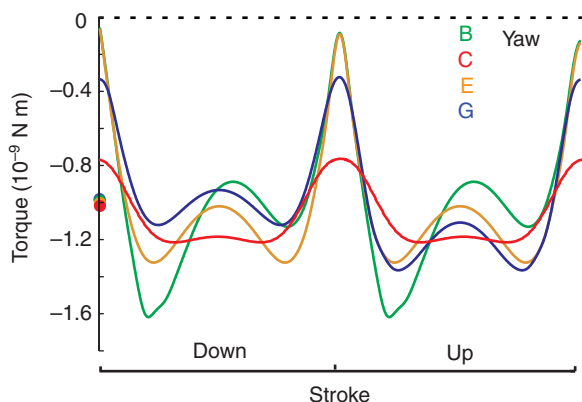

Fig. 6. Yaw FCT production using different wing kinematics: kinematics B (green), C (red), E (yellow) and G (blue).
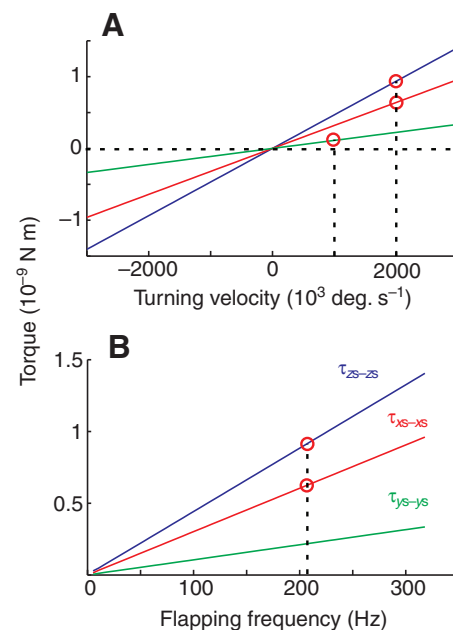

Fig. 7. FCT as a function of angular velocity and flapping frequency. The stroke-averaged value of FCTs is calculated for rotations about roll x_s (red), pitch y_s (green) and yaw z_s (blue) axes by (A) varying angular velocity and (B) varying the flapping frequency. Red circles indicate the conditions under which the values in Table 2 were calculated.

Table 3. Damping coefficients for the other five sets of free flight data (Fry et al., 2003)

Number of saccades	$\overline{C_N(\hat{t})}\cos(\varphi)\omega_{zs}$	$\overline{\omega_{zs}}$	C_{zs-zs}
Saccade 1	39.4	27.1	25.1
Saccade 2	−20.1	−16.2	21.5
Saccade 3	24.2	20.1	20.8
Saccade 4	36.2	32.7	19.2
Saccade 5	23.7	20.3	20.2
Saccade 6	23.3	20.9	19.3
Average	–	–	21.0

Averaging is based on the total duration of each saccade (excluding non-turning period). Dimensions for $\overline{\omega_{zs}}$ and C_{zs-zs} are $\mathrm{rad\,s^{-1}}$ and $10^{-12}\,\mathrm{N\,m\,s}$, respectively. $|\mathrm{d}\hat{\phi}/\mathrm{d}\hat{t}|$ is approximately equal to 4.3 (Ellington, 1984a). Other morphological data are listed in appendix C of Cheng et al., 2009.

Damping during free-flight saccades

Based on Eqn 7, we estimated the damping coefficients using six different sets of free-flight saccade data (Fry et al., 2005). The results are summarized in Table 3. The averaged value of yaw damping C_{zs-zs} is $21.00\times10^{-12}\,\mathrm{N\,m\,s}$, which is somewhat lower than the value provided by the simulation ($26.84\times10^{-12}\,\mathrm{N\,m\,s}$). This discrepancy could be due to the simplifications made in the simulations (quasi-steady aerodynamics, simplified turning dynamics and wing kinematics). Despite these uncertainties, the measured values are in good agreement.

We then replayed one set of saccade data (saccade 1, Table 3) using the robotic wing to investigate how body rotational velocity influences aerodynamic torque production. We compared the body frame yaw torque generated by two sets of wing kinematics in the presence (total yaw torque) and absence of body rotation (active yaw torque) (Fig. 3). We further divided the time trace of the saccade into four phases (Fig. 8) based on hovering (phase I), acceleration (phase II), constant body yaw velocity (phase III) and deceleration (phase IV). The corresponding damping coefficients during phases II, III and IV are calculated individually (Table 4). It can be seen that despite the differences between each period, the values of the yaw damping coefficients are quite close.

The active yaw torque measured in the current experiment is similar to that of a previous CFD study (Ramamurti and Sandberg, 2007), but appears to be smaller than the one measured by Fry et al. (Fry et al., 2003). However, except for a short period of phase III (see Discussion), all three studies suggest an active yaw torque that overestimates the total yaw torque (in the presence of body rotation) (Fig. 8A,B). This result indicates that body rotation causes non-negligible passive aerodynamic damping, as predicated by the FCT model. Notably, during realistic saccades, flies produce high angular velocities not only about the yaw axis but also about the roll and pitch axes (Fry et al., 2003; Schilstra and Van Hateren, 1999). The combined body angular velocity influences aerodynamic forces acting on the wings and causes the discrepancy between the active and total torques. In addition, the estimated total yaw torque (Fig. 8B) based on the Newton–Euler equation (Eqn 9) is very close to the one measured in our experiment (except in phase III; see Discussion for possible error sources).

It can be seen from Fig. 8 that both active and total yaw torques reach their peaks at phase II. In order to accelerate, the fruit fly needs to overcome not only body inertia but also the increasing damping due to FCT. During phase III, yaw angular velocity reaches a maximum and remains roughly constant in the particular case examined in this study. Therefore, at this period, a maximum damping is produced and overcome by the active yaw torque.
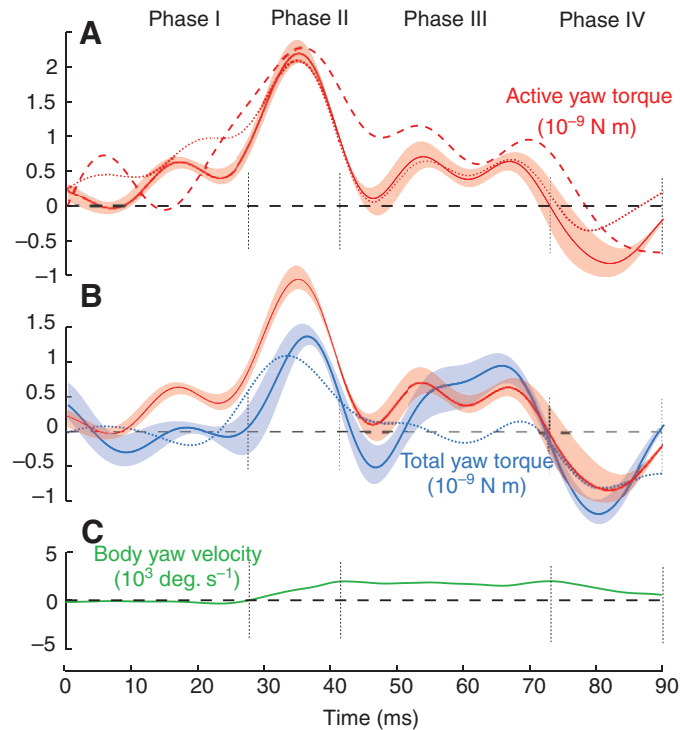

Fig. 8. Aerodynamic torques during a free-flight saccade. (A) Measured body yaw torque using wing kinematics in the absence of body velocity (solid red), compared with the previous CFD results [dotted red (Ramamurti and Sandberg, 2007)] and Fry's results [dashed red (Fry et al., 2003)]. (B) Estimation of total body yaw torque by the Euler equation (dotted blue), compared with the measured torque in the presence (solid blue) and absence (again, solid red) of body velocity. Because the cross-term in the Euler equation (Eqn 9) is negligible compared with the other terms, the estimated yaw torque is expected to be proportional to the yaw angular acceleration. (C) Body yaw angular velocity. The results are all represented in body coordinates.

However, the active yaw torque is reduced to less than half of its maximum value (in phase II, Fig. 8A,B). This indicates that upon acceleration (phase II), a larger amount of yaw torque is produced to overcome the body inertia than the damping. During phase IV, the fly is decelerating and it takes approximately two wing beats (about 9.5 ms) to decelerate to half the maximum angular velocity [as predicted in a parallel study (Hedrick et al., 2009)] and the entire deceleration lasts about 20 ms. The time constant calculated based on the damping coefficients listed in Table 4 is around 19 ms (I_{yaw}/C_{zb-zs}, $C_{zb-zs}\approx C_{zs-zs}$), indicating that passive damping could be largely responsible for the measured deceleration. Therefore, at this stage, the fly may employ wing kinematics with less asymmetry

Table 4. Damping coefficients for the first set of free flight data (Fry et al., 2003)

Period of saccade	$\overline{C_N(\hat{t})}\cos(\varphi)\omega_{zs}$	$\overline{\omega_{zs}}$	C_{zs-zs}
28–42 ms (phase II)	16.3	9.8	28.8
42–73 ms (phase III)	49.5	36.2	23.7
73–90 ms (phase IV)	35.8	21.8	28.4
28–90 ms	39.4	27.1	25.1

Averaging is based on the different periods of the saccade, and the total duration is 60 ms (30–90 ms, Fig. 8).

than in the acceleration phase as passive damping serves to reduce a large portion of the fly's angular velocity. This is evidenced by a study on the same sequence of flight data [figure 6 in Ramamurti and Sandberg (Ramamurti and Sandberg, 2007)]. Notably, despite the dominance of passive damping in deceleration, a small amount of active decelerating torque was observed in all three studies (solid, dotted and dashed red curves, phase IV, Fig. 8A), implying that active deceleration from asymmetric wing motion may work to terminate the turning.

DISCUSSION
Inertia or damping-dominated turning

We found that the saccade dynamics of *Drosophila* are affected by both FCT-induced passive aerodynamic damping and body inertia. Specifically, at the onset of the saccade, a fly needs to actively produce yaw torque to overcome both inertia and damping to accelerate. To decelerate, passive damping can account for most of the deceleration, while an active decelerating torque contributes to stop the turning and stabilize flight. As indicated by Eqn 1, the FCT model predicts an exponential decay of angular velocity; thus, for a complete stop of turning, an active counter-torque is required.

Based on the simulation results, the total damping coefficient (27.36×10^{-12} N m s, body frictional damping plus passive damping due to FCT) is more than 50 times that of the body alone (0.52×10^{-12} N m s), reducing the time constant to about 17 ms ($\tau = I_{yaw}/C_{zb-zs}$, I_{yaw} is the moment of inertia about the yaw axis, estimated at 0.49×10^{-12} N m s^2). This result is confirmed by the estimations based on the free-flight data (Tables 3 and 4), which give slightly higher time constants (19 ms for the saccade data used in the experiment) than the value based on the simulation. During a saccade, a fly decelerates from its maximum angular velocity to near zero angular velocity within about 20 ms; the time constant corresponds to an exponential decay of the yaw velocity to a value of $1/e$ (or 37%) of the original yaw velocity. The calculated time constant of 17 ms therefore corresponds to a reduction of the yaw velocity from 2000 deg. s^{-1} to 740 deg. s^{-1}. To decelerate the fly to less than 100 deg. s^{-1} [also see yaw velocity before saccades in Fry et al. (Fry et al., 2003)] would take a total of 51 ms, which is considerably longer than the deceleration duration measured in free flight (e.g. phase IV, Fig. 8C). Thus, a small amount of counter-torque due to active wing control is required to terminate body rotation.

In summary, passive wing damping accounts largely, but not entirely, for saccade termination. This view is consistent with the wing kinematics during free-flight saccades measured by Fry et al. (Fry et al., 2003), which showed pronounced active steering during the acceleration phase and a somewhat weaker counter-steering during the deceleration phase of a saccade. The role of active mechanisms is further supported by experiments comparing the time course of saccades measured on rigid tethers with those measured on loose tethers (Mayer et al., 1988; Bender and Dickinson, 2006a). The prolonged saccade durations of rigidly tethered flies, which lack meaningful mechanosensory feedback from the halteres, suggests that flies utilize active sensory-motor reflexes to terminate saccades. The halteres are likely sources of this mechanosensory feedback; increasing the sensitivity of the halteres (by adding mass) results in shorter saccades, whereas decreasing sensitivity (by ablating one haltere) results in longer saccades on a magnetic tether (Bender and Dickinson, 2006b). As an alternative explanation, haltere feedback might be used to simply terminate the kinematics that created the torque to turn – returning the wings to a symmetrical pattern – without triggering active counter-torque production. However, all previous studies of haltere-induced reflexes suggest that the halteres trigger compensatory reactions, i.e. counter-torque to resist imposed angular rotation (Bender and Dickinson, 2006a; Bender and Dickinson, 2006b; Dickinson et al., 1999).

Banked turn in saccades

Measurements of free-flight saccades indicate that both fruit flies (Fry et al., 2003) and blowflies (Schilstra and Van Hateren, 1999) bank during saccadic turns. It is observed that, at the start of turning, a fly tends to rotate about its body yaw axis (Fig. 1), not the vertical axis in the inertial frame (the body pitch angle is roughly 45 deg. inclined relative to the horizontal plane), and this causes a rolling motion of the insect because of the coupling of the Euler angles. This turning pattern might be due to an interesting feature of torque production during a saccade; that is, body yaw torque is mainly produced during the upstroke, while most of the body roll torque is produced during the downstroke. The reason is that during the upstroke the force created by the wing is nearly orthogonal to the fly's body yaw axis (Fry et al., 2003), and during the downstroke the force is roughly orthogonal to the body roll axis. As the saccade continues, the fly deviates from its regular body orientation, and it starts to stabilize itself by actively producing aerodynamic torque, while the passive damping due to FCT about the roll and pitch axes is also likely to contribute.

Flight stability

During hovering or cruising flight, flies tend to maintain a constant yaw angle, except during saccadic turns (Collett and Land, 1975). This constancy could be attributed to a strong optomotor response (Varju, 1990) and haltere feedback (Dickinson et al., 1999; Sherman and Dickinson, 2003) to induce active stabilizing torques. In the current study, we found that FCT, as a passive mechanism, produces a strong restoring torque that acts in the opposite direction of rotation. We have analyzed here the body rotation-induced aerodynamic damping at hovering conditions and found it to be crucial in saccades with low translational body velocity. To explain the role of FCT in flight stability, a previous study calculated the linearized attitude dynamics for the hovering condition, but the results were inconclusive (Cheng et al., 2009). Other studies on hovering longitudinal dynamics (Sun and Xiong, 2005; Taylor and Thomas, 2003) indicated that insect flight is likely to be inherently unstable. However, a comprehensive experimental or theoretical study to determine the stability of flight dynamics is lacking.

During forward/backward, sideways or vertical flight, it is highly possible that body translation will induce a similar damping effect to that due to body rotation. For example, forward/backward body velocities will impart an asymmetry on wing velocities during upstroke and downstroke, resulting in a net drag (averaged over one wing stroke) under symmetric wing motions (Appendix 2):

$$\overline{\Delta F_D} = -\rho S R \hat{r}_1^1(S) \Phi n C_D(\hat{t}) \left| \frac{d\hat{\phi}}{d\hat{t}} \right| \cos^2(\phi) v_{xs} , \qquad (11)$$

where $\hat{r}_1^1(S)$ is non-dimensional first moment of wing area, $C_D(\hat{t})$ is (mean sectional) drag coefficient at non-dimensional time $\hat{t}$ (Dickson and Dickinson, 2004), and v_{xs} is the forward/backward velocity in the stroke plane frame. In correspondence with FCT, we termed this net drag (Eqn 11) flapping counter-force (FCF). It is easy to see that FCF will further induce a net pitch torque around the center of gravity, which is generally located below the wing base. This type of pitch torque together with the FCT is likely to cause instability in the longitudinal dynamics (B.C. and X.D., in preparation).

The effect of aerodynamic damping – whether in rotational or translational motion, is to reduce the relative velocity between the insect and air. In still air, FCT is able to passively damp out the body angular velocity, and therefore may enhance flight stability and alleviate some work from the sensory-motor system to generate rapid active responses. An interesting question arises related to air turbulence. While FCT enhances flight stability in stationary air, it could have converse effects in turbulent air; namely, to drag the fly along with the surrounding air flow. We consider externally induced air turbulence to be relatively insignificant at the size scale of a fly's wing due to air viscosity (tiny vortices would disappear almost immediately), however, and dismiss a significant effect of air turbulence and FCT for this reason. FCF, on the other hand, is likely to be greatly affected by external turbulence (typically with large translational velocity) at a significantly larger scale compared with the fly size, and may drag the fly into the surrounding air.

Limitations and error sources in the current study

In this study, we first investigated FCT based on quasi-steady aerodynamics. We only considered translational aerodynamic force due to delayed stall and neglected other aerodynamic mechanisms such as rotational lift and wake capture. We further simplified the analysis by assuming a fixed center of pressure on the wing. By making those simplifications, we were able to give a simple and intuitive mathematical description for the FCT mechanism (Eqns 3–7) and illustrate its linearity (Fig. 7). The effect of the neglected aerodynamic mechanisms is investigated in a subsequent study (B.C. and X.D., in preparation), while we study the FCT mechanisms during roll, pitch and yaw rotations through a series of robotic wing experiments.

Firstly, in the robotic wing experiments to replay the saccade data, the error mainly arose from the measurement of body and wing kinematics. The kinematics were extracted from the calibrated videos by tracking the markers on the insect's head, tail, wing base and tip. In particular, measurement of the fly's body roll depended on the difficult measurement of the wing hinge positions, which could be measured with limited precision. A calculation of roll velocity amplifies any measurement error. In phase III of the analyzed flight data (Fig. 8), the calculated roll angular velocity [not shown, refer to figure 8C in Cheng et al. (Cheng et al., 2009)] has a large oscillation, and we suspect it may reflect an amplified measurement error. In contrast, the large roll oscillation during phase III could also affect the measurement of wing kinematics during this phase (the spanwise vectors of the wing were calculated by subtracting the position of wing hinge from that of the wing tip). We also consider the wing kinematics in the body-centered frame may have better accuracy compared with that in the inertial frame, since the body kinematics were subtracted from the former. Overall, the above error may cause the discrepancy (especially in phase III) between the measured total yaw torque (solid blue, Fig. 8B) and its predication by the Newton–Euler equation (dotted blue, Fig. 8B).

Secondly, the error arises from the robotic wing experiment to replay the exact the wing trajectory measured. Specifically, error might come from the PID control of the DC brush motors, the inevitable gap between the gears and the zero-drift of sensor. Neglecting the wing–wing interaction and the uncertainties of morphological parameters (such as wing flexing, relative body movement) may also affect the results. Furthermore, we didn't consider the translational velocity of the insect's body. Although the set of saccade used is near hovering (with a small ascending), a small amount of translational velocity still existed during turning

(see figure 2A in Fry et al. [Fry et al., 2003]), especially, during phases III and IV.

Despite these possible sources of error, we consider they have limited effects on our results and do not affect the main conclusions. The active yaw torque measured in the current experiment closely matches the CFD results (Ramamurti and Sandberg, 2007), and all three studies [including that of Fry et al. (Fry et al., 2003)] suggest non-negligible passive damping induced by body rotation.

APPENDIX 1

The gravitational force and torque of the wing are calculated and subtracted from the measured aerodynamic force and torque. The magnitude of the resultant value F_{robot} and τ_{robot} are then scaled to the force on the actual fly F_{fly} and τ_{fly} according to the following equations (Sane, 2001):

$$F_{\text{fly}} = F_{\text{robot}} \frac{\rho_{\text{air}}\, n_{\text{fly}}^2\, S_{\text{fly}}\, r_2^2(S)_{\text{fly}}}{\rho_{\text{oil}}\, n_{\text{robot}}^2\, S_{\text{robot}}\, r_2^2(S)_{\text{robot}}} \tag{A1}$$

$$\tau_{\text{fly}} = \tau_{\text{robot}} \frac{R_{\text{fly}}}{R_{\text{robot}}} . \tag{A2}$$

APPENDIX 2

The net drag induced by forward/backward body velocity can be directly obtained based on previous results (Dickson and Dickinson, 2004). By applying blade element theory, the instantaneous drag acting on a wing can be expressed as [equation 8 in Dickson and Dickinson (Dickson and Dickinson, 2004)]:

$$\left| F_{\text{D}}(\hat{t}) \right| = \frac{1}{2} C_{\text{D}}(\hat{t}) \rho S R^2 \left(\frac{d\phi}{dt} \right)^2 \left[\hat{r}_2^2(s) + 2\hat{r}_1^1(S)\mu + \mu^2 \right], \tag{B1}$$

where μ is the advance ratio defined as:

$$\mu = \frac{v_{xs} \cos(\phi)}{R(d\phi/dt)} . \tag{B2}$$

In backward motions (positive v_{xs}, refer to Fig. 1), μ is negative during downstroke (negative $d\phi/dt$) and positive during upstroke (positive $d\phi/dt$) (*vice versa* for forward motion). By averaging over one wing stroke, the net drag of a wing pair is:

$$\overline{\Delta F_{\text{D}}} = -2\rho S R^2 \hat{r}_1^1(S) \overline{C_{\text{D}}(\hat{t}) \left(\frac{d\phi}{dt} \right)^2 \mu \cos(\phi)} =$$

$$-\rho S R \hat{r}_1^1(S) \Phi n \overline{C_{\text{D}}(\hat{t}) \left| \frac{d\hat{\phi}}{d\hat{t}} \right| \cos^2(\phi)} v_{xs} . \tag{B3}$$

LIST OF SYMBOLS

$\bar{c}$	mean chord length
C_{D}	drag coefficient
C_{i-j}	damping coefficient about i axis during rotation about j axis
C_{N}	normal force coefficient
m	body mass
n	flapping frequency
$\hat{r}_1^1(S)$	non-dimensional first moment of wing area
$\hat{r}_2^2(S)$	non-dimensional second moment of wing area
$\hat{r}_{\text{cp}}$	normalized center of pressure on the wing
R	wing length
Re	Reynolds number
S	wing area
$\hat{t}$	non-dimensional time
v_{xs}	forward/backward velocity in the stroke plane frame
x_{b}	body roll axis

x_s	roll axis in the stroke plane frame
y_b	body pitch axis
y_s	pitch axis in the stroke plane frame
z_b	body yaw axis
z_s	yaw axis in the stroke plane frame
α	angle of attack
θ	stroke deviation
Θ	maximum stroke deviation
Θ_0	offset of stroke deviation
ν	kinematic viscosity
ρ	fluid/air density
τ_{pitch}	FCT during pitch rotation
τ_{roll}	FCT during roll rotation
τ_{yaw}	FCT during yaw rotation
ϕ	stroke angle
φ	rotation angle
Φ	flapping amplitude
ψ	maximum rotation angle
χ_0	free body angle
ω_{xs}	roll angular velocity in the stroke plane frame
ω_{ys}	pitch angular velocity in the stroke plane frame
ω_{zs}	yaw angular velocity in the stroke plane frame

ACKNOWLEDGEMENTS

REFERENCES

Bender, J. A. and Dickinson, M. H. (2006a). Comparison of visual and haltere-mediated feedback in the control of body saccades in *Drosophila melanogaster*. *J. Exp. Biol.* **209**, 4597-4606.

Bender, J. A. and Dickinson, M. H. (2006b). Visual stimulation of saccades in magnetically tethered *Drosophila*. *J. Exp. Biol.* **209**, 3170-3182.

Cheng, B., Fry, S. N., Huang, Q., Dickson, W. B., Dickinson, M. H. and Deng, X. (2009). Turning dynamics and passive damping in flapping flight. In *Proceedings of IEEE International Conference on Robotics and Automation*, pp.1889-1896. Kobe, Japan.

Collett, T. S. and Land, M. F. (1975). Visual control of flight behaviour in the hoverfly *Syritta pipiens* L. *J. Comp. Physiol. A* **99**, 1-66.

Deng, X. Y., Schenato, L., Wu, W. C. and Sastry, S. S. (2006). Flapping flight for biomimetic robotic insects: Part I – System modeling. *IEEE Trans. Rob.* **22**, 776-788.

Dickinson, M. H., Lehmann, F. O. and Sane, S. P. (1999). Wing rotation and the aerodynamic basis of insect flight. *Science* **284**, 1954-1960.

Dickson, W. B. and Dickinson, M. H. (2004). The effect of advance ratio on the aerodynamics of revolving wings. *J. Exp. Biol.* **207**, 4269-4281.

Dudley, R. (1990). Biomechanics of flight in neotropical butterflies-morphometrics and kinematics. *J. Exp. Biol.* **150**, 37-53.

Dudley, R. (1991). Biomechanics of flight in neotropical butterflies-aerodynamics and mechanical power requirements. *J. Exp. Biol.* **159**, 335-357.

Ellington, C. P. (1984a). The aerodynamics of hovering insect flight. *Phil. Trans. R. Soc. Lond. B* **305**, 1-181.

Ellington, C. P. (1984b). The aerodynamics of hovering insect flight. VI. Lift and power requirements. *Phil. Trans. R. Soc. Lond. B* **305**, 145-181.

Ennos, A. R. (1989). The kinematics and aerodynamics of the free flight of some diptera. *J. Exp. Biol.* **142**, 49-85.

Fry, S. N., Sayaman, R. and Dickinson, M. H. (2003). The aerodynamics of free-flight maneuvers in *Drosophila. Science* **300**, 495-498.

Fry, S. N., Sayaman, R. and Dickinson, M. H. (2005). The aerodynamics of hovering flight in *Drosophila. J. Exp. Biol.* **208**, 2303-2318.

Fry, S. N., Rohrseitz, N., Straw, A. D. and Dickinson, M. H. (2008). TrackFly: Virtual reality for a behavioral system analysis in free-flying fruit flies. *J. Neurosci. Methods* **171**, 110-117.

Götz, K. G. (1987). Course-control, metabolism and wing interference during ultralong tethered flight in *Drosophila melanogaster. J. Exp. Biol.* **128**, 35-46.

Hedrick, T. L. (2008). Software techniques for two- and three-dimensional kinematic measurements of biological and biomimetic systems. *Bioinspiration Biomimetics* **3**, 6.

Hedrick, T. L., Cheng, B. and Deng, X. (2009). Wingbeat time and the scaling of passive rotational damping in flapping flight. *Science* **324**, 252-255.

Heisenberg, M. and Wolf, R. (1979). On the fine structure of yaw torque in visual flight orientation of *Drosophila melanogaster. J. Comp. Physiol. A* **130**, 113-130.

Heisenberg, M. and Wolf, R. (1988). Reafferent control of optomotor yaw torque in *Drosophila melanogaster. J. Comp. Physiol. A* **163**, 373-388.

Hesselberg, T. and Lehmann, F. O. (2007). Turning behaviour depends on frictional damping in the fruit fly *Drosophila. J. Exp. Biol.* **210**, 4319-4334.

Land, M. F. and Collett, T. S. (1974). Chasing behaviour of houseflies (*Fannia canicularis*). *J. Comp. Physiol. A* **89**, 331-357.

Mayer, M., Vogtmann, K., Bausenwein, B., Wolf, R. and Heisenberg, M. (1988). Flight control during free yaw turns in *Drosophila melanogaster. J. Comp. Physiol. A* **163**, 389-399.

Murray, R. M., Li, Z. and Sastry, S. S. (1994). *A Mathematical Introduction To Robotic Manipulation.* New York: CRC press.

Ramamurti, R. and Sandberg, W. C. (2002). A three-dimensional computational study of the aerodynamic mechanisms of insect flight. *J. Exp. Biol.* **205**, 1507-1518.

Ramamurti, R. and Sandberg, W. C. (2007). A computational investigation of the three-dimensional unsteady aerodynamics of *Drosophila* hovering and maneuvering. *J. Exp. Biol.* **210**, 881-896.

Reichardt, W. and Poggio, T. (1976a). Visual control of orientation behavior in fly. 1. Quantitative-analysis. *Q. Rev. Biophys.* **9**, 311-375.

Reichardt, W. and Poggio, T. (1976b). Visual control of orientation behavior in fly. 2. Towards underlying neural interactions. *Q. Rev. Biophys.* **9**, 377-438.

Ribak, G. and Swallow, J. G. (2007). Free flight maneuvers of stalk-eyed flies: do eye-stalks affect aerial turning behavior? *J. Comp. Physiol. A* **193**, 1065-1079.

Sane, S. P. (2001). The aerodynamics of flapping wings. PhD thesis, Integrative Biology, University of California, Berkeley.

Sane, S. P. and Dickinson, M. H. (2001). The control of flight force by a flapping wing: lift and drag production. *J. Exp. Biol.* **204**, 2607-2626.

Sane, S. P. and Dickinson, M. H. (2002). The aerodynamic effects of wing rotation and a revised quasi-steady model of flapping flight. *J. Exp. Biol.* **205**, 1087-1096.

Schilstra, C. and Van Hateren, J. H. (1999). Blowfly flight and optic flow. I. Thorax kinematics and flight dynamics. *J. Exp. Biol.* **202**, 1481-1490.

Sherman, A. and Dickinson, M. H. (2003). A comparison of visual and haltere-mediated equilibrium reflexes in the fruit fly *Drosophila melanogaster. J. Exp. Biol.* **206**, 295-302.

Sun, M. and Wang, J. K. (2007). Flight stabilization control of a hovering model insect. *J. Exp. Biol.* **210**, 2714-2722.

Sun, M. and Xiong, Y. (2005). Dynamic flight stability of a hovering bumblebee. *J. Exp. Biol.* **208**, 447-459.

Tammero, L. F. and Dickinson, M. H. (2002). Collision-avoidance and landing responses are mediated by separate pathways in the fruit fly, *Drosophila melanogaster. J. Exp. Biol.* **205**, 2785-2798.

Taylor, G. K. and Thomas, A. L. R. (2003). Dynamic flight stability in the desert locust *Schistocerca gregaria. J. Exp. Biol.* **206**, 2803-2829.

Tobalske, B. W. (2009). Evolution: symmetry in turns, *Science* **324**, 190-191.

Varju, D. (1990). A note on the reafference principle. *Biol. Cybern.* **63**, 315-323.

Zhao, L., Huang, Q., Deng, X. and Sane, S. P. (2009). The effect of chord-wise flexibility on the aerodynamic force generation of flapping wings: Experimental studies. In *Proceedings of IEEE International Conference on Robotics and Automation*, pp.4207-4212. Kobe, Japan.